Check for updates

Theoretical insights into the electroreduction of nitrate to ammonia on graphene-based single-atom catalysts†

Yuanyuan Wang,[a,b] Donghai Wu,[a,b,c] Peng Lv,[a,b] Bingling He,[a,b] Xue Li,[a,b] Dongwei Ma [ID] *[a,b] and Yu Jia [ID] *[a,b,d]

Electrocatalytic reduction of harmful nitrate (NO_3^-) to valuable ammonia (eNO$_3$RR) is critical and attractive for both environmental remediation and energy transformation. A single atom catalyst (SAC) based on graphene represents one of the most promising eNO$_3$RR catalysts. However, the underlying catalytic mechanism and the intrinsic factors dictating the catalytic activity trend remain unclear. Herein, using first-principles calculations, eNO$_3$RR on TMN$_3$ and TMN$_4$ (TM = Ti–Ni) doped graphene was thoroughly investigated. Our results reveal that FeN$_4$ doped graphene exhibits excellent eNO$_3$RR performance with a low limiting potential of −0.38 V, agreeing with the experimental finding, which can be ascribed to the effective adsorption and activation of NO_3^- via the charge "acceptance–donation" mechanism and its moderate binding due to the occupation of the d–p antibonding orbital. In particular, we found that eNO$_3$RR activities are well correlated with the intrinsic properties of TM centers and their local environments. With the established activity descriptor, several other graphene-based SACs were efficiently screened out with excellent eNO$_3$RR performance. Our studies could not only provide an atomic insight into the catalytic mechanism and activity origin of eNO$_3$RR on graphene-based SACs, but also open an avenue for the rational design of SACs for eNO$_3$RR towards ammonia by regulating the metal center and its local coordination environment.

1. Introduction

Ammonia (NH$_3$) is not only one of the most fundamental industrial chemicals but also acts as an emerging energy storage medium and carbon-free energy carrier.[1,2] For more than one century, NH$_3$ synthesis in industry has mainly relied on the Haber–Bosch technology operating under harsh conditions. Considering that the Haber–Bosch process is both energy- and capital-intensive, in recent years the electrochemical synthesis of NH$_3$ through the nitrogen reduction reaction (NRR), driven by renewable energy, has attracted great

research interest.[3,4] However, generally the NRR suffers from an unsatisfactory conversion rate and low faradaic efficiency, resulting from the extremely inert N$_2$ molecule.[5,6] Given the much weaker N=O bond (204 kJ mol^{-1}) and N–O bond (176 kJ mol^{-1}) than the N≡N bond (941 kJ mol^{-1}), very recently, other nitrogen resources, including nitrate (NO_3^-), nitrite (NO_2^-), and nitric oxide (NO), have attracted more and more attention for NH$_3$ synthesis.[7,8] As the third-largest accessible form of nitrogen[9] and most oxidized reactive nitrogen,[10] NO_3^- has been considered as one of the most widespread water pollutants in the world.[11,12] Under this circumstance, the electrocatalytic NO_3^- reduction reaction (eNO$_3$RR) to produce NH$_3$ is considered as a promising alternative to the NRR because it can simultaneously remediate environmental pollution and yield valuable NH$_3$ potentially more efficiently than the NRR.[13,14]

Rational design of the electrocatalyst with excellent activity, high selectivity, and long durability is critical for the development of a practical eNO$_3$RR device. Encouragingly, various catalysts, such as molecular solids,[13] pure metals,[7,15,16] metallic alloys,[17–19] metal compounds,[20–23] and atomic catalysts,[24–34] have been demonstrated to be highly efficient for eNO$_3$RR. For example, it is shown that, at −0.4 V versus the reversible hydro-

[a]*Key Laboratory for Special Functional Materials of Ministry of Education, and School of Materials Science and Engineering, Henan University, Kaifeng 475004, China. E-mail: madw@henu.edu.cn, jiayu@henu.edu.cn*
[b]*Joint Center for Theoretical Physics, and Center for Topological Functional Materials, Henan University, Kaifeng 475004, China*
[c]*Henan Key Laboratory of Nanocomposites and Applications, Institute of Nanostructured Functional Materials, Huanghe Science and Technology College, Zhengzhou 450006, China*
[d]*International Laboratory for Quantum Functional Materials of Henan, and School of Physics, Zhengzhou University, Zhengzhou 450001, China*
†Electronic supplementary information (ESI) available. See DOI: https://doi.org/10.1039/d2nr02813a

gen electrode, an NH_3 production rate of $436 \pm 85\ \mu g\ h^{-1}\ cm^{-2}$ and ultrahigh faradaic efficiency of 85.9% can be achieved on the copper–molecular solid catalyst.[13] Single atom catalysts (SACs), such as TMN_3 and TMN_4-doped graphene (denoted as $TMN_3@G$ and $TMN_4@G$, respectively), have attracted huge attention in electrocatalysis due to their unique electronic and geometric structures as well as high stability.[35,36] For eNO_3RR, several SACs have been experimentally reported to be excellent,[24–28] and theoretically predicted to be promising.[29–33] For example, $FeN_4@G$ can exhibit an NH_3 yield rate of up to $\sim20\,000\ \mu g\ h^{-1}\ mg_{cat.}^{-1}$ and a maximal faradaic efficiency of $\sim75\%$.[25]

Besides the common merits of SACs, graphene-based SACs can be considered as an ideal platform for understanding the fundamental physical chemistry of a specific reaction from first-principles calculations, due to the distinct geometric and electronic characteristics of the graphene support.[37] Moreover, the coordination environment of the TM center embedded in graphene can be purposely tuned *via* direct and indirect coordination engineering, which produces huge numbers of SAC systems and makes graphene-based SACs find various potential applications, especially for electrocatalysis.[38,39] As discussed above, until now only $FeN_4@G$ has been investigated for eNO_3RR towards NH_3.[25] Thus, the investigation of eNO_3RR catalyzed by graphene-based SACs is still in its infancy, and it is urgent to unravel the underlying catalytic mechanism and activity origin, and identify the intrinsic factors dictating their catalytic activity trend, guided by which high performance graphene-based SACs for eNO_3RR can be rationally designed effectively.

Based on the above considerations, herein we systematically studied the eNO_3RR on $TMN_3@G$ and $TMN_4@G$ (TM = Ti, V, Cr, Mn, Fe, Co, Ni, and Cu), through first-principles calculations. The detailed reaction pathway for the electroreduction of NO_3^- into NH_3 was explored thoroughly, to illustrate the activity and selectivity. It is found that $FeN_4@G$ stands at the top of the volcano among $TMN_4@G$ with a limiting potential (U_L) −0.38 V, and exhibits the highest eNO_3RR performance, in agreement with the experimental findings.[25] In addition, among $TMN_3@G$, $CoN_3@G$ exhibits the highest eNO_3RR performance with U_L of −0.65 V. Then, the eNO_3RR activity origin was investigated through electronic structure analysis. Finally, an intrinsic descriptor to uncover the eNO_3RR activity trend for the graphene-based SAC was proposed, which correlates with the local environment of the TM atom, *i.e.*, its electronegativity and coordination number, and the electronegativity of its nearest neighbor atoms. The identified descriptor is distinct from the previously proposed one, that is, the binding free energy of NO_3^- $(\Delta G(NO_3^*))$,[29–33] which is based on energies that are hard to measure and modulate in experiments. In addition, guided by the proposed descriptor, several other graphene-based SACs with high eNO_3RR performance were efficiently screened out, and especially the non-noble metal Ni SAC coordinated with one nitrogen and two carbon atoms exhibits a high intrinsic activity with U_L of −0.41 V.

2. Computational details

In this work, spin-polarized first-principles calculations were carried out using Vienna *Ab initio* Simulation Package (VASP).[40] The projector augmented wave (PAW) method was employed to account for the electron–ion interactions.[41] The exchange–correlation effect was described by the Perdew–Burke–Ernzerhof (PBE) functional within the generalized gradient approximation (GGA).[42] The cutoff energy for the plane-wave basis set was taken as 450 eV. The Grimme's DFT-D3 method was adopted to account for the van der Waals interaction.[43] The energy and force convergence criteria for the geometry optimizations were set as 10^{-5} eV and 0.02 eV $Å^{-1}$, respectively. The Brillouin zone of the $7 \times 7 \times 1$ graphene supercell was sampled by $3 \times 3 \times 1$ and $6 \times 6 \times 1$ k-point meshes for structural optimization and calculation of densities of states (DOS), respectively. A vacuum thickness of ~20 Å was placed along the z direction to minimize the interaction between periodic units. The thermal stability was estimated through *ab initio* molecular dynamics (AIMD) simulations.

According to the computational hydrogen electrode (CHE) model,[44] the Gibbs free energy change (ΔG) for each elemental step was calculated by

$$\Delta G = \Delta E + \Delta E_{ZPE} - T\Delta S.$$

In the equation, ΔE was directly obtained from DFT calculations. ΔE_{ZPE} and $T\Delta S$ $(T = 298.15\ K)$ are the contributions of zero-point energy and entropy, respectively, which were acquired by computing the vibrational frequency of intermediates, as listed in Table S1,† while ΔE_{ZPE} and $T\Delta S$ of the free molecules were taken from the NIST database (Table S2†).[45] For the CHE model, for the reaction $A^* + H^+ + e^- \rightarrow AH^*$, the free energy change is calculated according to $G(AH^*) - [\mu(H^+) + \mu(e^-)] - G(A^*)$. The CHE model shows that the chemical potential of a proton–electron pair $[(\mu(H^+) + \mu(e^-)]$ at zero potential can be regarded as half the chemical potential of the free H_2 molecule $[1/2\mu(H_2)]$, *i.e.*, $\mu(H^+) + \mu(e^-) = 1/2\mu(H_2)$. Based on this model, $G(AH^*) - [\mu(H^+) + \mu(e^-)] - G(A^*)$ can be calculated as $G(AH^*) - 1/2\mu(H_2) - G(A^*)$. U_L is formulized with $U_L = \Delta G_{max}/e$, where ΔG_{max} is the free energy change of the potential-determining step (PDS).[46] When computing the binding free energy of NO_3^- $(\Delta G(NO_3^*))$, the gaseous HNO_3 was adopted as a reference, and due to that directly calculating the energy of charged NO_3^- is difficult.[47,48] Then $\Delta G(NO_3^*)$ was obtained by

$$\Delta G(NO_3^*) = G(NO_3^*) - G^* - [G(HNO_3) - 1/2G(H_2)] + \Delta G_{correct}$$

in which $\Delta G(NO_3^*)$ and G^* are the Gibbs free energy of the NO_3 adsorbed SACs and the pristine SACs, respectively. $G(HNO_3)$ and $G(H_2)$ denote the Gibbs free energy of gaseous HNO_3 and H_2 molecules, respectively. The free energy correction, $\Delta G_{correct}$, is set as 0.392 eV.[47,48] The solvation effect, realized by the implicit solvation model,[49] on the free energy during the reaction process has been tested for $FeN_4@G$. As presented below, the U_L and reaction pathway are insensitive

to solvation correction. Therefore, we did not consider the solvation effect for the other systems, as done in previous works.[29,31]

3. Results and discussion

3.1. NO_3^- adsorption

$TMN_3@G$ and $TMN_4@G$ have been widely studied both experimentally and theoretically for various catalytic reactions, especially the electrocatalysis reaction because the graphene support has a large surface area, excellent conductivity, and high (electro)-chemical stability. $TMN_3@G$ and $TMN_4@G$ feature TM single atoms that are coordinated with three and four pyridine nitrogen atoms, respectively, in the graphene matrix, which could significantly influence their activity, selectivity, and stability, due to the strong electronic-metal support interaction.[50,51] Typical atomic configurations of $TMN_3@G$ and $TMN_4@G$ are presented in Fig. 1 and S1a, S1b,† and seven TMs (Ti, V, Cr, Mn, Fe, Co, and Ni) have been considered as the catalytic active center. The key parameters of these systems are compiled in Table S3,† such as TM–N bond lengths, charge transfers,[52] and spin magnetic moments, which agree well with previous studies.[53] The total DOS for all these SACs presented in Fig. S1c and S1d† suggest their metallic characteristics, beneficial to the charge transfer during eNO_3RR.[30]

Effective adsorption of NO_3^- is a prerequisite to trigger the eNO_3RR process. Hence, we first investigated the adsorption behavior of NO_3^- on these SACs. Various adsorption configurations have been considered with one or two O atoms bonded with TM centers, and the most stable ones are shown in Fig. 2a, for which the key structural parameters are displayed in Table S4.† We can see that on $TMN_3@G$, NO_3^- tends to be adsorbed *via* two O atoms, while on $TMN_4@G$, NO_3^- prefers to

be adsorbed *via* one O atom, except TiN_4 and $VN_4@G$. Accordingly, the values of $\Delta G(NO_3^*)$ (Table S4†) indicate that for the same TM, $TMN_3@G$ possesses higher NO_3^- binding strength than $TMN_4@G$, and for the same coordination the adsorption strength gradually decreases with the active center changing from Ti to Ni. Then the charge transfer from the supports to NO_3^- was calculated (Table S4†). From Fig. 2b, we can see that there is a good linear correlation between the charge gained by the adsorbates and their binding strengths to $TMN_3@G$, *i.e.*, the more strongly NO_3^- binds, the more negatively charged they are.[29,30] In contrast, the correlation between the charge of the adsorbates and the binding strengths for $TMN_4@G$ is rather poor, which may result from the distinct adsorption configurations of NO_3^- on different $TMN_4@G$, as shown in Fig. 2a. The different correlations between NO_3^- binding strength on $TMN_3@G$ and $TMN_4@G$ reflect the coordination environment effects.

Moreover, in solution, the hydrogen evolution reaction (HER) is the main competing reaction against eNO_3RR. To effectively suppress the HER, NO_3^- should be bonded more strongly than H.[29,30] We, therefore, studied the adsorption of H atoms on all the investigated systems, for which the optimized structures are presented in Fig. S2.† As shown in Fig. 2c, for all the cases the binding free energy of H* ($\Delta G(H^*)$) is much more positive than $\Delta G(NO_3^*)$, indicating that the active site will be preferentially occupied by NO_3^- rather than H, and thus the HER can be effectively suppressed.

3.2. Reaction mechanism of eNO_3RR

Although eNO_3RR is complicated and potentially has a variety of products (such as NO_2, NO, N_2O, and N_2), the Pourbaix diagram of nitrogen species indicates that NH_3/NH_4^+ is the most stable product in thermodynamics under the negative electrode potential.[29,54] Thus, it is quite necessary to fully explore the detailed reaction process of NO_3^- electroreduction
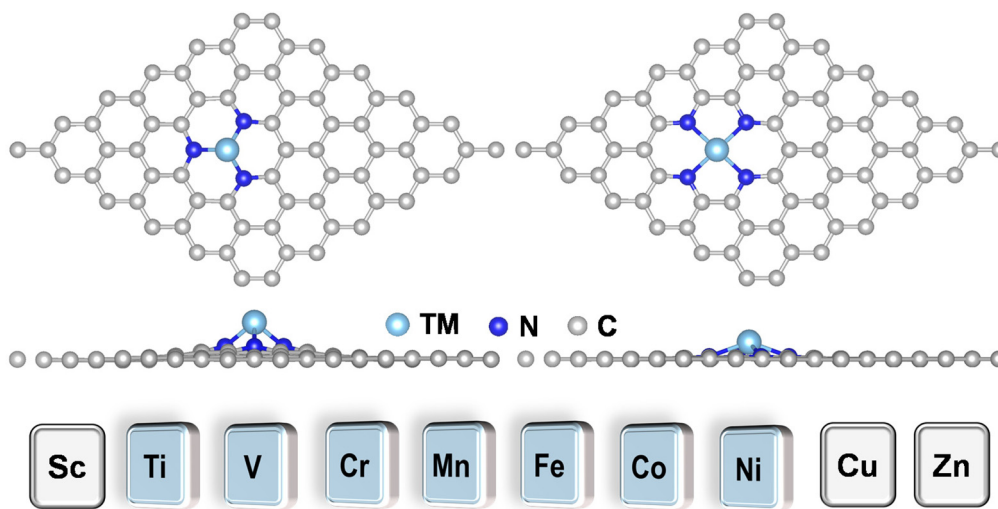

Fig. 1 Typical atomic configurations of the $TMN_3@G$ (left) and $TMN_4@G$ (right) systems. The considered TM atoms include Ti, V, Cr, Mn, Fe, Co, and Ni.
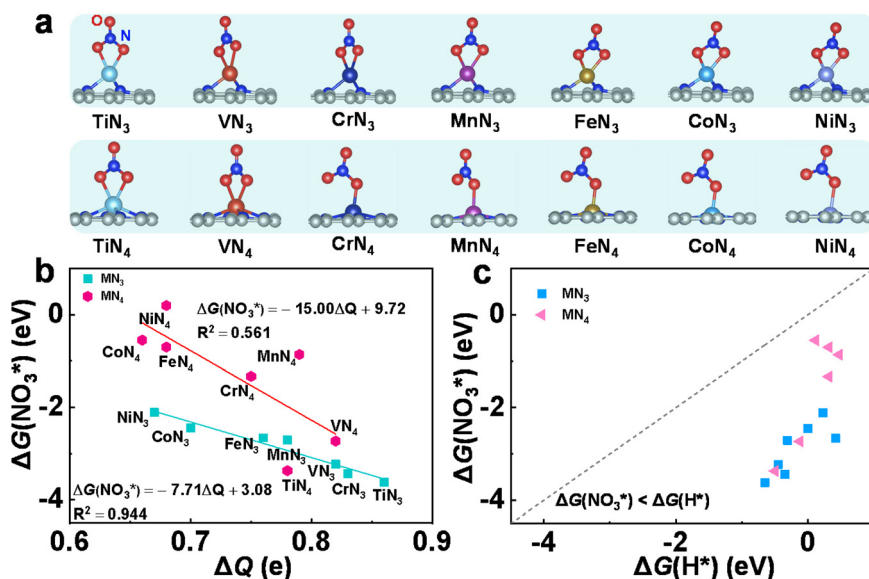
Fig. 2 (a) Atomic configurations of the TMN_3@G (upper panel) and TMN_4@G (lower panel) with the adsorbed NO_3^-. (b) The relationship between charge transfer (ΔQ) of the NO_3^- and its binding free energy ($\Delta G(NO_3^*)$). (c) Comparison of the binding free energies of NO_3^- ($\Delta G(NO_3^*)$) and H atom ($\Delta G(H^*)$).

into NH_3. Given that there are multiple adsorption structures and hydrogenation positions of intermediates, during the eNO_3RR process the most stable intermediates in each elementary step have been selected for further reaction to efficiently screen out the optimal eNO_3RR pathway on TMN_3@G and TMN_4@G. The adsorption configurations of the key intermediate, NO*, are displayed in Fig. S3.† In most cases, NO adsorption adopts the N-end pattern with the N atom bonded with the TM atom, suggesting that the N-end pathway proposed previously should be feasible.[29,30] The calculated U_L values and the corresponding PDS are summarized in Fig. 3. Interestingly, for most systems, $OH^* + H^+ + e^- \rightarrow * + H_2O$ is the PDS, and the strongly bonded OH* group could lead to catalyst poisoning.
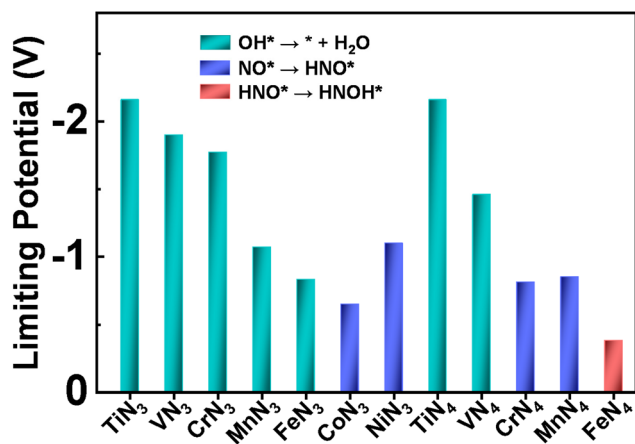

Fig. 3 Summary of the limiting potential and potential-determining step for eNO_3RR on various SACs along the most favorable pathway.

Moreover, generally U_L exhibits a general decreasing trend changed from early TM to late TM for both TMN_3 and TMN_4@G. Importantly, CoN_3 and FeN_4@G exhibit the highest eNO_3RR activity among the considered TMN_3@G and TMN_4@G systems, respectively. The PDS of CoN_3 and FeN_4@G are $NO^* + H^+ + e^- \rightarrow HNO^*$ and $HNO^* + H^+ + e^- \rightarrow HNOH^*$ with U_L values of -0.65 and -0.38 V, respectively. Note that the full reaction pathways of CoN_4 and NiN_4@G systems have not been studied, due to that they are unable to effectively capture the key reaction intermediate (NO_3H^*), as shown in Fig. S4.†

To get insight into the reaction mechanism of eNO_3RR, the reaction pathways on CoN_3 and FeN_4@G are presented in Fig. 4, and those for the other systems in Fig. S5–S14.† Firstly, NO_3^- is adsorbed on CoN_3@G (Fig. 4a) and FeN_4@G (Fig. 4b) with two O–Co bonds and one O–Fe bond, respectively, with $\Delta G(NO_3^*)$ values of -2.45 and -0.70 eV. Distinct binding strengths of NO_3^- will lead to different activation and different free energy changes in the first hydrogenation step. Interestingly, the first proton–electron pair prefers to attack the O atom of NO_3^* bonded with Co (Fe) rather than the terminal O atom. Consequently, one N–O bond is cleaved to form $NO_2^* + OH^*$ on CoN_3@G with an energy release of -0.72 eV, while on FeN_4@G, NO_3H^* is formed with an energy input of 0.23 eV. The second hydrogenation step leads to the formation of a H_2O molecule. The intermediate, NO_2^*, binds with the Co atom via two Co–O bonds, while it binds with the Fe atom with the Fe–N bond, and the processes are exothermic by 0.82 and 2.28 eV, respectively, on CoN_3 and FeN_4@G. The subsequent proton–electron pair transfer leads to the hydrogenation of NO_2^*. On CoN_3@G, $NO^* + OH^*$ is formed with a free energy uphill of 0.44 eV, while, on FeN_4@G, NO_2H^* is formed with a free energy downhill of 0.08 eV. Following this, they are
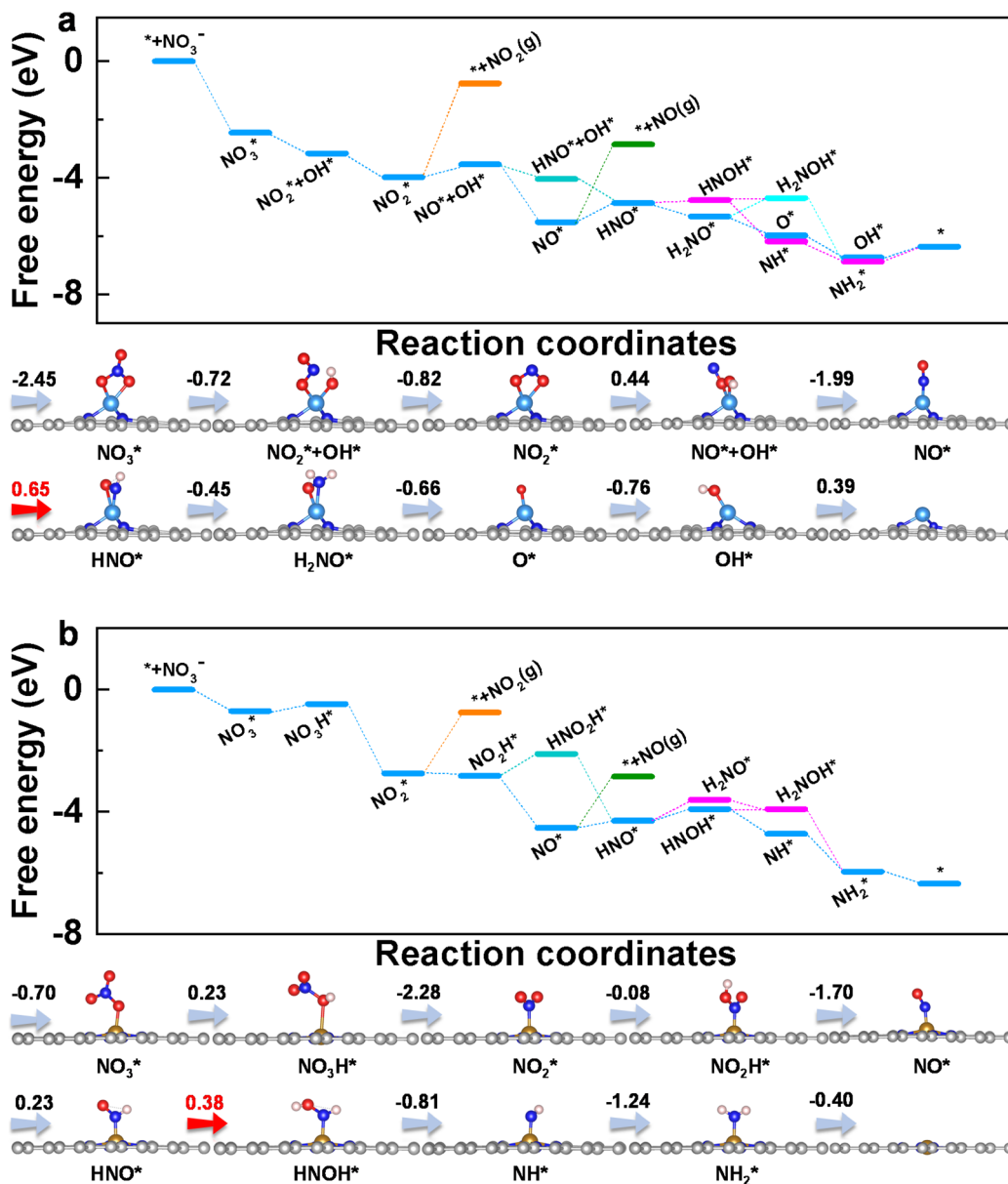
Fig. 4 Free energy diagrams and corresponding intermediates of eNO$_3$RR on CoN$_3$@G (a) and FeN$_4$@G (b). The pathways to release of NO$_2$ and NO are also plotted for comparison.

attacked by the proton–electron pair to release the H$_2$O molecule and leave NO* on both CoN$_3$ and FeN$_4$@G, with an energy change of −1.99 and −1.70 eV, respectively. On both systems, NO* prefers the end-on adsorption pattern, and is hydrogenated to form HNO* species. For CoN$_3$@G, the hydrogenation of NO* needs an energy input of 0.65 eV, and the following hydrogenation of HNO* prefers to undergo the consecutive pathway to release the NH$_3$ molecule through HNO* → H$_2$NO* → O* + NH$_3$ with the energy release of 1.11 eV. In addition, after the formation of HNO*, all the electrochemical steps are endothermic along the preferred pathways. Therefore, NO* → HNO* is the PDS and eNO$_3$RR on CoN$_3$@G possesses a limiting potential of −0.65 V. In contrast, as shown in Fig. 4b, NO*

is hydrogenated to HNO* with a free energy change of 0.23 eV, and then HNO* is preferably hydrogenated to HNOH* with a free energy uphill of 0.38 eV. Due to this all the remaining elemental reaction steps are exothermic along the preferred pathways, HNO* → HNOH* is the PDS with a low limiting potential of −0.38 V, which agrees well with the experimental findings.[25]

Above, we have demonstrated that the HER can be well suppressed on CoN$_3$ and FeN$_4$@G. In addition to the HER, we further examined the possible formation of other byproducts along the eNO$_3$RR reaction pathways. As shown in Fig. 4a, both NO and NO$_2$ are tightly bonded on CoN$_3$@G with the desorption energy barriers of 2.68 and 3.22 eV, respectively, indi-

cating the significantly difficult formation of these byproducts. In contrast, the hydrogenation of NO$_2$* and NO* requires much less energy, further confirming that both species will be further hydrogenated rather than desorbed. Similarly, for FeN$_4$@G (Fig. 4b), the desorption of NO and NO$_2$ is also very difficult, as indicated by the large desorption energy barriers of 1.69 and 1.99 eV, respectively, while their hydrogenation is even exothermic (−0.08 eV for NO$_2$* → NO$_2$H* and 0.23 eV for NO* → HNO*). Considering that NO* is bonded with the metal center *via* the N atom only, the NO dimer may be formed through a couple of N–Co (Fe) bonds, which could lead to the production of N$_2$.[29–33] However, due to that NO is strongly adsorbed on CoN$_3$ and FeN$_4$@G, the formation of the NO dimer will need to overcome a large energy barrier. In fact, in ref. 25 the Faraday efficiencies of N$_2$ and H$_2$ are less than 1%, and thus our theoretical studies on eNO$_3$RR selectivity provide a good explanation of the experimental findings. In addition, the desorption of NH$_3$ is exothermic (−0.4 eV) on FeN$_4$@G and slightly endothermic by 0.4 eV on CoN$_3$@G, indicating that both systems can be easily recovered for the NO$_3^-$ to NH$_3$ electroreduction cycle. Finally, the solvation effect has been investigated for eNO$_3$RR on FeN$_4$@G, simulated by the implicit solvation model implemented in VASPsol.[49] The free energy diagram is presented in Fig. S15.† It can be seen that the reaction pathway and PDS are the same as in the case without solvation correction, and U_L is only lowered by 0.03 V.

3.3. Activity origin of eNO$_3$RR

In the following, the eNO$_3$RR activity origin of CoN$_3$ and FeN$_4$@G is discussed based on the electronic structure analysis, and then the key factors affecting the eNO$_3$RR activity trend of graphene-based SACs was revealed. The adsorption and activation of NO$_3^-$ is the prerequisite for its further hydrogenation, and the moderate binding strength is crucial for achieving high eNO$_3$RR activity, according to the Sabatier principle. As shown in Fig. 5a and b, FeN$_4$ and CoN$_3$@G possess considerable spin magnetic moment localized on the embedded Fe (2.03μ_B) and Co (2.11μ_B) atoms, respectively. This localized spin magnetic moment of SACs and its associated spin-unpaired electrons could play an important for the adsorption and activation of small molecules, as suggested by previous studies.[55,56] Accordingly, as shown in Table S4,† NiN$_4$@G that possesses a nonmagnetic ground state is unable to effectively bind NO$_3^-$ with a binding free energy of 0.20 eV. The charge redistributions owing to NO$_3^-$ adsorption for FeN$_4$ and CoN$_3$@G are also displayed in Fig. 5a and b, respectively, where the yellow and cyan regions denote electron accumulation and depletion, respectively. On the whole, electrons are transferred from the catalysts to NO$_3$*, in line with the Bader analysis,[52] which shows that NO$_3$* obtains ∼0.7e electrons for both systems. In detail, the electrons (yellow region) obtained by NO$_3$* mainly occupy its antibonding orbitals, while besides the supports, NO$_3$* also loses some charges (cyan region) from its bonding orbitals. Therefore, NO$_3$* is effectively activated for the further hydrogenation reaction *via* the charge "acceptance–donation" mechanism, similar to the case of N$_2$ activation in the NRR.[57]

Furthermore, the orbital interaction between NO$_3$* and its bonded Fe or Co was investigated. The projected DOS for the FeN$_4$ and CoN$_3$@G are presented in Fig. 5c and d, respectively, and the others in Fig. S16.† We can see that, in a large energy range, 3d states of the Fe or Co effectively interact with 2p states of O of NO$_3$*. Furthermore, interestingly, crystal orbital Hamilton populations (COHP)[58] calculations show that for
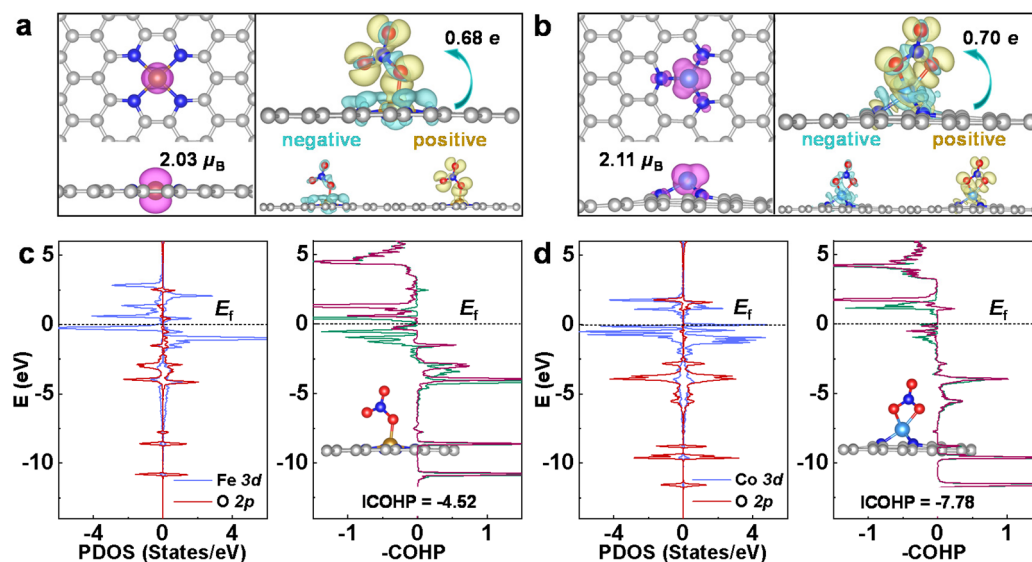
Fig. 5 (a) Spin density distribution of the pristine FeN$_4$@G and charge density difference of the FeN$_4$@G with the adsorbed NO$_3^-$. (b) is similar to (a), except that it is for CoN$_3$@G. (c) Projected densities of states (PDOS) of the Fe 3d states and O 2p states, which is bonded with Fe, and the COHP for the interaction between NO$_3^-$ and Fe. (d) is similar to (c), except that it is for the NO$_3^-$ adsorbed CoN$_3$@G. In (a) and (b), the yellow and cyan regions denote electron accumulation and depletion, respectively, and the isosurface value is set to 0.002 e per bohr^3. In (c) and (d), Fermi level (E_f) is set to 0 eV.

FeN$_4$@G there are significant d–p antibonding states occupied below the Fermi level, while for CoN$_3$@G the occupation of the d–p antibonding states is much less, which gives integrated COHP (ICOHP) of −4.52 and −7.78, respectively, for FeN$_4$ and CoN$_3$@G. The less negative ICOHP means weaker chemical bonding interaction, and thus the COHP analysis verifies the calculated binding strength trend of NO$_3^-$ on FeN$_4$ and CoN$_3$@G. As discussed in previous works[29–33] and in the following herein, the moderate binding of NO$_3^-$ is crucial for the high eNO$_3$RR activity. Thus, the occupied antibonding states near the Fermi level could play an important role in mediating the binding strength of NO$_3$* on FeN$_4$@G appropriately to achieve high eNO$_3$RR activity.

According to the Sabatier principle, either too strong or too weak adsorption of the reaction intermediates goes against the whole catalytic process. This empirical principle has been turned into a quantitative predictive tool with the improvement of the accuracy of DFT calculatios.[59] Currently, the binding free energy of the key intermediate has been often taken as the descriptor for various reactions to predict the activity trend and guide the catalyst design.[60–62] As for eNO$_3$RR, previous studies indicate that $\Delta G(NO_3*)$ can be adopted as an effective descriptor.[29–33] Herein, as shown in Fig. 6a, although exhibiting different activity trend, the U_L values of both TMN$_3$@G and TMN$_4$@G are well correlated with $\Delta G(NO_3*)$. For TMN$_3$@G, CoN$_3$@G locates at the peak of the activity volcano, while for TMN$_4$@G, Fe$_4$@G at the peak of the

activity volcano, considering that Co$_4$ and Ni$_4$@G should have low catalytic activity due to the considerably low chemical activity to capture the key intermediate as discussed above. In addition, from Fig. 3, we note that too strong adsorption of NO$_3^-$ means that the active sites possess too high chemical activity, which tend to overbind OH*, leading to OH* → * + H$_2$O as the PDS and high U_L (including TiN$_3$, VN$_3$, CrN$_3$, MnN$_3$, FeN$_3$, TiN$_4$, and VN$_4$@G). On the other hand, relatively weak adsorption of NO$_3^-$ on the catalysts leads to NO* → HNO* or HNO* → HNOH* as the PDS with lower U_L (such as CoN$_3$, CrN$_4$, MnN$_4$, and FeN$_4$@G).

As $\Delta G(NO_3*)$ can serve as a good activity descriptor, it is necessary to identify the properties of the catalysts that determine it. It has been well-established in surface science and heterogeneous catalysis that the binding strength of an adsorbate on a metal surface correlates with the d-band center of the atoms to which the adsorbate binds.[63,64] This conclusion also holds for the present case. As shown in Fig. 6b, there are good linear relationships between the d-band center of the embedded TM (Fig. S17†) and the binding free energies of NO$_3^-$ with different trends for TMN$_3$@G and TMN$_4$@G. It is noted that the binding energy of the adsorbate is hard to measure and control, while the d-band center can be accessible experimentally by using synchrotron-based high-resolution photoemission spectroscopy and tuned by various means.[65,66] However, the descriptor that only includes the intrinsic physical and chemical properties without resorting to theoretical calcu-
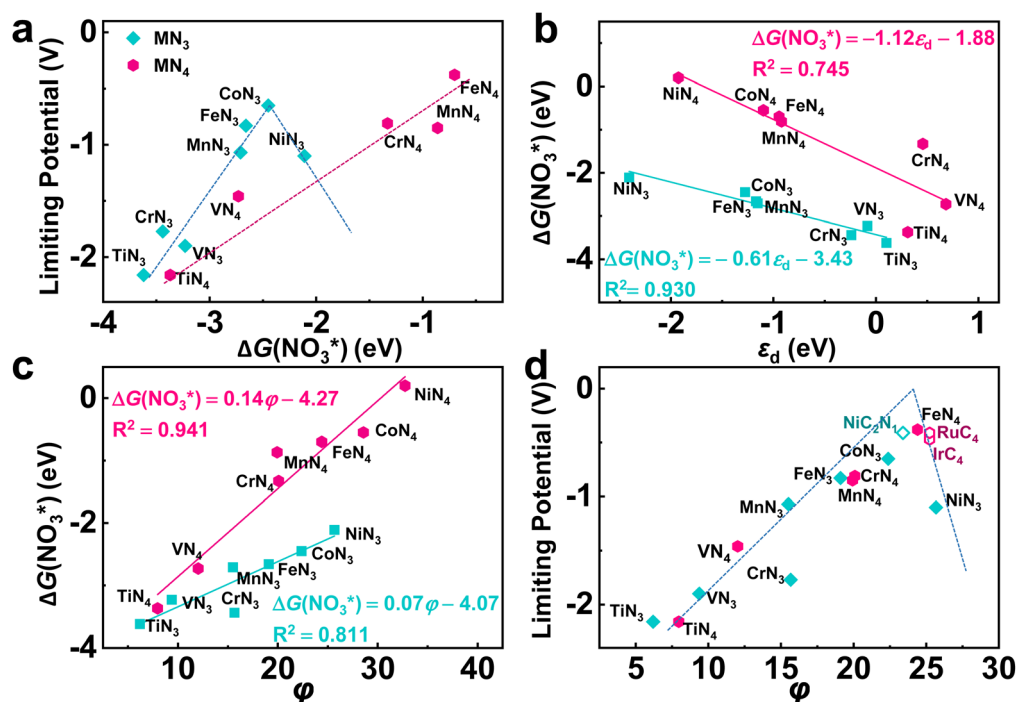
Fig. 6 (a) Relationship between the binding free energy of NO$_3^-$ ($\Delta G(NO_3*)$ and the limiting potential for the considered TMN$_3$@G and TMN$_4$@G systems. (b) Relationship between the d-band center (ε_d) of the embedded TM atom and $\Delta G(NO_3*)$. (c) Relationship between the φ values of the catalysts and $\Delta G(NO_3*)$. (d) Activity volcano plot for the eNO3RR on the considered graphene-based SACs with φ as the activity descriptor. The dashed lines in (a) and (d) is used to guide the eyes.

lations or experimental measurements is more preferable. So, we consider the descriptor, φ, proposed by Xu et al.,[67] which can be verified by the d-band center model and defined as

$$\varphi = \theta_d \times \frac{E_M + \alpha \times (n_N \times E_N + n_C \times E_C)}{E_O}$$

where E_M, E_N, and E_C denote the electronegativity of metal, nitrogen, and carbon elements, respectively; n_C and n_N represent the number of C and N atoms coordinated with the TM atoms; θ_d is the valence electrons in the occupied d orbital of the TM element derived from the periodic table of elements; E_O is the electronegativity of oxygen element; and α is taken as 1. Interestingly, as shown in Fig. 6c, $\Delta G(NO_3^*)$ for TMN_3@G and TMN_4@G are correlated linearly with φ having R^2 values of 0.811 and 0.941, respectively. The strong linear correlation suggests that φ can function as an efficient descriptor to predict the eNO$_3$RR catalytic activity. As expected, as shown in Fig. 6d, the U_L of eNO$_3$RR indeed exhibits a volcano relationship with φ, and importantly φ is a unified descriptor for both TMN_3@G and TMN_4@G systems. Moreover, compared with the commonly adopted energy- and orbital-based descriptor, φ relates to the basic properties of catalysts, including the coordination number, and the electronegativity of the TM active center and its coordinated atoms. Thus, it is convenient to use φ to predict the eNO$_3$RR activity of the graphene-based SACs, compared with $\Delta G(NO_3^*)$ or the d-band center.

Taking φ as a guide, we further studied the eNO$_3$RR activity of graphene-based SACs in other coordination environments, including $TMC_{3-x}N_x$@G (x = 0–2) and $TMC_{4-x}N_x$ (x = 0–3). In particular, NiC$_2$N$_1$, RuC$_4$, and IrC$_4$@G, possessing φ values of 23.4, 25.23, and 25.23 respectively, locate near the high-activity region. Therefore, the eNO$_3$RR reaction pathways for these three systems were further explored in detail. Interestingly, our

calculated results show that NiC$_2$N$_1$, RuC$_4$, and IrC$_4$@G indeed follow the volcano relationship presented in Fig. 6d, with U_L values of −0.41, −0.41, and −0.47 V respectively. The free energy diagram and atomic configuration of intermediates are presented in Fig. 7 for NiC$_2$N$_1$@G, and Fig. S18 and S19† for RuC$_4$ and IrC$_4$@G, respectively. From Fig. 7, NiC$_2$N$_1$@G not only exhibits high intrinsic eNO$_3$RR activity but also excellent selectivity against other products, and thus is a promising candidate with low cost for efficient electro conversion of NO$_3^-$ to NH$_3$. Considering that NiC$_2$N$_1$@G has been synthesized,[68] this descriptor guided eNO$_3$RR catalyst design strategy could be experimentally verified in the future.

In addition, small amounts of NO$_2^-$ may coexist with NO$_3^-$ in the solution.[69] Therefore, we studied the binding strengths of NO$_2^-$ ($\Delta G(NO_2^*)$) for the systems of CoN$_3$, FeN$_4$, NiC$_2$N$_1$, RuC$_4$, and IrC$_4$@G, which exhibit relatively high eNO$_3$RR activity. The values of $\Delta G(NO_3^*)$ for CoN$_3$, FeN$_4$, NiC$_2$N$_1$, RuC$_4$, and IrC$_4$@G are −2.45, −0.70, −1.86, −1.85, and −1.73 eV, respectively. The values of $\Delta G(NO_2^*)$ for CoN$_3$, FeN$_4$, NiC$_2$N$_1$, RuC$_4$, and IrC$_4$@G are −2.38, −1.14, −1.60, −1.64, and −1.64 eV, respectively. We can see for FeN$_4$@G that NO$_2^-$ binds more strongly than NO$_3^-$. Therefore, there may be competition between the electrocatalytic reduction of NO$_2^-$ and NO$_3^-$. However, as shown in Fig. 4b, NO$_2^*$ is the intermediate of eNO$_3$RR. In particular, the PDS for eNO$_3$RR on FeN$_4$@G is the hydrogenation of HNO*, which means that the reduction of NO$_2^-$ follows the same paths as eNO$_3$RR. Therefore, if there is NO$_2^-$ in the solution, NO$_2^-$ will be reduced first to produce NH$_3$, and then NO$_3^-$ will be reduced to produce NH$_3$. In other words, FeN$_4$@G is a bifunctional electrocatalyst for reducing both NO$_2^-$ and NO$_3^-$ to yield NH$_3$.

Finally, it is noted that Ling et al. have performed a systematic theoretical study on the NRR on the graphene-based

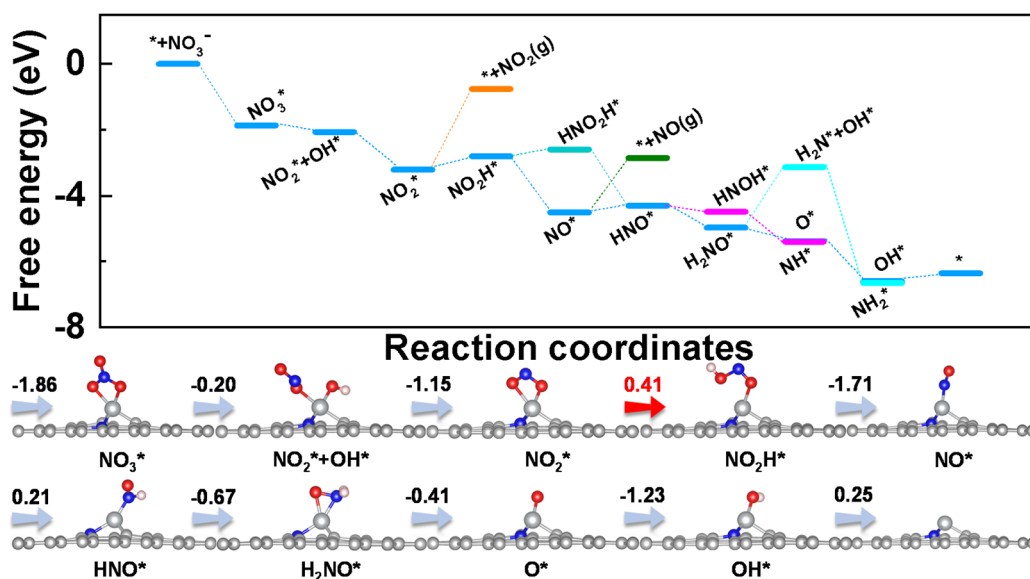**Fig. 7** Free energy diagrams and corresponding intermediates of eNO$_3$RR on NiC$_2$N$_1$@G. The pathways to release of NO$_2$ and NO are also plotted for comparison.

SACs with the computational settings consistent with ours.[53] Comparing this work with ours, the main differences between the NRR and eNO$_3$RR on the graphene-based SACs can be summarized as follow. From ref. 53, we can see that for the graphene-based SACs the active sites for the NRR are early transition metals with less d electrons and high activity, including Nb, W, Re, V, Zr, and Mo, except that there is one system with Ru as the active site. This is in sharp contrast with the situation of eNO$_3$RR. From our theoretical results, the active centers of the SACs with high NO$_3$RR activity are late transition metals with more d electrons and low chemical activity, such as Fe, Ni, Ru, and Ir. The reason for this difference is that the N$_2$ molecule is extremely inert and hard to be activated, while NO$_3^-$ can be easily activated, due to the much larger bond energy of N$_2$ compared with NO$_3^-$.

4. Conclusion

In conclusion, eNO$_3$RR on TMN$_3$@G and TMN$_4$@G SACs has been systematically studied by means of first-principles calculations. The calculated results show that FeN$_4$@G exhibits high eNO$_3$RR activity (U_L = −0.38 V) and excellent NH$_3$ selectivity to suppress the formation of byproducts, including other nitrogen-containing molecules and H$_2$. The activity origin can be traced back to the effective adsorption and activation of NO$_3^-$ via the charge "acceptance–donation" mechanism and its moderate binding due to the occupation of the d–p antibonding orbital. These theoretical results provide a deep understanding of the excellent eNO$_3$RR performance of FeN$_4$@G demonstrated in the experiments.[25] More importantly, it is found that the eNO$_3$RR activities of TMN$_3$@G and TMN$_4$@G SACs are well correlated with their intrinsic properties. The established activity descriptor, φ, including the coordination number, and the electronegativity of the TM center and its co-ordinated atoms, can be conveniently used to guide the design of graphene-based SACs for efficient eNO$_3$RR. Finally, taking φ as a guide, several other graphene-based SACs were efficiently screened out with excellent eNO$_3$RR performance. Our studies provide an atomic understanding of the catalytic mechanism and activity origin of the eNO$_3$RR on graphene-based SACs, and further highlight the importance of the metal center and its local coordination environment for tuning the eNO$_3$RR performance of SACs.

Conflicts of interest

The authors declare no conflict of interest.

Acknowledgements

References

1 D. Bao, Q. Zhang, F.-L. Meng, H.-X. Zhong, M.-M. Shi, Y. Zhang, J.-M. Yan, Q. Jiang and X.-B. Zhang, *Adv. Mater.*, 2017, **29**, 1604799.

2 J. W. Erisman, M. A. Sutton, J. Galloway, Z. Klimont and W. Winiwarter, *Nat. Geosci.*, 2008, **1**, 636–639.

3 S. L. Foster, S. I. P. Bakovic, R. D. Duda, S. Maheshwari, R. D. Milton, S. D. Minteer, M. J. Janik, J. N. Renner and L. F. Greenlee, *Nat. Catal.*, 2018, **1**, 490–500.

4 B. H. R. Suryanto, H.-L. Du, D. Wang, J. Chen, A. N. Simonov and D. R. MacFarlane, *Nat. Catal.*, 2019, **2**, 290–296.

5 B. Ma, H. Zhao, T. Li, Q. Liu, Y. Luo, C. Li, S. Lu, A. M. Asiri, D. Ma and X. Sun, *Nano Res.*, 2021, **14**, 555–569.

6 Y. Ren, C. Yu, X. Tan, H. Huang, Q. Wei and J. Qiu, *Energy Environ. Sci.*, 2021, **14**, 1176–1193.

7 Y. Wang, W. Zhou, R. Jia, Y. Yu and B. Zhang, *Angew. Chem., Int. Ed.*, 2020, **59**, 5350–5354.

8 J. Long, S. Chen, Y. Zhang, C. Guo, X. Fu, D. Deng and J. Xiao, *Angew. Chem., Int. Ed.*, 2020, **59**, 9711–9718.

9 J. G. Chen, R. M. Crooks, L. C. Seefeldt, K. L. Bren, R. M. Bullock, M. Y. Darensbourg, P. L. Holland, B. Hoffman, M. J. Janik, A. K. Jones, M. G. Kanatzidis, P. King, K. M. Lancaster, S. V. Lymar, P. Pfromm, W. F. Schneider and R. R. Schrock, *Science*, 2018, **360**, eaar6611.

10 Z. Wang, D. Richards and N. Singh, *Catal. Sci. Technol.*, 2021, **11**, 705–725.

11 C. Yu, X. Huang, H. Chen, H. C. J. Godfray, J. S. Wright, J. W. Hall, P. Gong, S. Ni, S. Qiao, G. Huang, Y. Xiao, J. Zhang, Z. Feng, X. Ju, P. Ciais, N. C. Stenseth, D. O. Hessen, Z. Sun, L. Yu, W. Cai, H. Fu, X. Huang, C. Zhang, H. Liu and J. Taylor, *Nature*, 2019, **567**, 516–520.

12 X. Zhang, Y. Wang, C. Liu, Y. Yu, S. Lu and B. Zhang, *Chem. Eng. J.*, 2021, **403**, 126269.

13 G.-F. Chen, Y. Yuan, H. Jiang, S.-Y. Ren, L.-X. Ding, L. Ma, T. Wu, J. Lu and H. Wang, *Nat. Energy*, 2020, **5**, 605–613.

14 H. Xu, Y. Ma, J. Chen, W.-X. Zhang and J. Yang, *Chem. Soc. Rev.*, 2022, **51**, 2710–2758.

15 J. Li, G. Zhan, J. Yang, F. Quan, C. Mao, Y. Liu, B. Wang, F. Lei, L. Li, A. W. M. Chan, L. Xu, Y. Shi, Y. Du, W. Hao, P. K. Wong, J. Wang, S.-X. Dou, L. Zhang and J. C. Yu, *J. Am. Chem. Soc.*, 2020, **142**, 7036–7046.

16 Q. Hu, Y. Qin, X. Wang, Z. Wang, X. Huang, H. Zheng, K. Gao, H. Yang, P. Zhang, M. Shao and C. He, *Energy Environ. Sci.*, 2021, **14**, 4989–4997.

17 Y. Wang, A. Xu, Z. Wang, L. Huang, J. Li, F. Li, J. Wicks, M. Luo, D.-H. Nam, C.-S. Tan, Y. Ding, J. Wu, Y. Lum, C.-T. Dinh, D. Sinton, G. Zheng and E. H. Sargent, *J. Am. Chem. Soc.*, 2020, **142**, 5702–5708.

18 H. Yin, Z. Chen, S. Xiong, J. Chen, C. Wang, R. Wang, Y. Kuwahara, J. Luo, H. Yamashita, Y. Peng and J. Li, *Chem. Catal.*, 2021, **1**, 1088–1103.

19 G. A. Cerrón-Calle, A. S. Fajardo, C. M. Sánchez-Sánchez and S. Garcia-Segura, *Appl. Catal., B*, 2022, **302**, 120844.

20 R. Jia, Y. Wang, C. Wang, Y. Ling, Y. Yu and B. Zhang, *ACS Catal.*, 2020, **10**, 3533–3540.

21 L. Wei, D.-J. Liu, B. A. Rosales, J. W. Evans and J. Vela, *ACS Catal.*, 2020, **10**, 3618–3628.

22 R. Daiyan, T. Tran-Phu, P. Kumar, K. Iputera, Z. Tong, J. Leverett, M. H. A. Khan, A. Asghar Esmailpour, A. Jalili, M. Lim, A. Tricoli, R.-S. Liu, X. Lu, E. Lovell and R. Amal, *Energy Environ. Sci.*, 2021, **14**, 3588–3598.

23 J. Liang, H. Chen, T. Mou, L. Zhang, Y. Lin, L. Yue, Y. Luo, Q. Liu, N. Li, A. A. Alshehri, I. Shakir, P. O. Agboola, Y. Wang, B. Tang, D. Ma and X. Sun, *J. Mater. Chem. A*, 2022, **10**, 6454–6462.

24 P. Li, Z. Jin, Z. Fang and G. Yu, *Energy Environ. Sci.*, 2021, **14**, 3522–3531.

25 Z.-Y. Wu, M. Karamad, X. Yong, Q. Huang, D. A. Cullen, P. Zhu, C. Xia, Q. Xiao, M. Shakouri, F.-Y. Chen, J. Y. Kim, Y. Xia, K. Heck, Y. Hu, M. S. Wong, Q. Li, I. Gates, S. Siahrostami and H. Wang, *Nat. Commun.*, 2021, **12**, 2870.

26 T. Zhu, Q. Chen, P. Liao, W. Duan, S. Liang, Z. Yan and C. Feng, *Small*, 2020, **16**, 2004526.

27 J. Wu, J.-H. Li and Y.-X. Yu, *J. Phys. Chem. Lett.*, 2021, **12**, 3968–3975.

28 Y. Zhang, X. Chen, W. Wang, L. Yin and J. C. Crittenden, *Appl. Catal., B*, 2022, **310**, 121346.

29 H. Niu, Z. Zhang, X. Wang, X. Wan, C. Shao and Y. Guo, *Adv. Funct. Mater.*, 2021, **31**, 2008533.

30 J. Wu, J.-H. Li and Y.-X. Yu, *J. Phys. Chem. Lett.*, 2021, **12**, 3968–3975.

31 L. Lv, Y. Shen, J. Liu, X. Meng, X. Gao, M. Zhou, Y. Zhang, D. Gong, Y. Zheng and Z. Zhou, *J. Phys. Chem. Lett.*, 2021, **12**, 11143–11150.

32 T. Hu, M. Wang, C. Guo and C. M. Li, *J. Mater. Chem. A*, 2022, **10**, 8923–8931.

33 L. Yang, S. Feng and W. Zhu, *J. Phys. Chem. Lett.*, 2022, **13**, 1726–1733.

34 P. Lv, D. Wu, B. He, X. Li, R. Zhu, G. Tang, Z. Lu, D. Ma and Y. Jia, *J. Mater. Chem. A*, 2022, **10**, 9707–9716.

35 Q. Zhang and J. Guan, *Nano Res.*, 2022, **15**, 38–70.

36 Y. Chen, S. Ji, C. Chen, Q. Peng, D. Wang and Y. Li, *Joule*, 2018, **2**, 1242–1264.

37 H.-Y. Zhuo, X. Zhang, J.-X. Liang, Q. Yu, H. Xiao and J. Li, *Chem. Rev.*, 2020, **120**, 12315–12341.

38 X. Li, H. Rong, J. Zhang, D. Wang and Y. Li, *Nano Res.*, 2020, **13**, 1842–1855.

39 J. Zhang, H. Yang and B. Liu, *Adv. Energy Mater.*, 2021, **11**, 2002473.

40 G. Kresse and J. Furthmüller, *Phys. Rev. B: Condens. Matter Mater. Phys.*, 1996, **54**, 11169–11186.

41 P. E. Blöchl, *Phys. Rev. B: Condens. Matter Mater. Phys.*, 1994, **50**, 17953–17979.

42 J. P. Perdew, J. A. Chevary, S. H. Vosko, K. A. Jackson, M. R. Pederson, D. J. Singh and C. Fiolhais, *Phys. Rev. B: Condens. Matter Mater. Phys.*, 1992, **46**, 6671–6687.

43 S. Grimme, J. Antony, S. Ehrlich and H. Krieg, *J. Chem. Phys.*, 2010, **132**, 154104.

44 J. K. Nørskov, J. Rossmeisl, A. Logadottir, L. Lindqvist, J. R. Kitchin, T. Bligaard and H. Jónsson, *J. Phys. Chem. B*, 2004, **108**, 17886–17892.

45 https://webbook.nist.gov/chemistry/.

46 X. Guo, J. Gu, S. Lin, S. Zhang, Z. Chen and S. Huang, *J. Am. Chem. Soc.*, 2020, **142**, 5709–5721.

47 J.-X. Liu, D. Richards, N. Singh and B. R. Goldsmith, *ACS Catal.*, 2019, **9**, 7052–7064.

48 F. Calle-Vallejo, M. Huang, J. B. Henry, M. T. M. Koper and A. S. Bandarenka, *Phys. Chem. Chem. Phys.*, 2013, **15**, 3196–3202.

49 K. Mathew, R. Sundararaman, K. Letchworth-Weaver, T. A. Arias and R. G. Hennig, *J. Chem. Phys.*, 2014, **140**, 084106.

50 Y. Peng, B. Lu and S. Chen, *Adv. Mater.*, 2018, **30**, 1801995.

51 C. Xia, Y. Qiu, Y. Xia, P. Zhu, G. King, X. Zhang, Z. Wu, J. Y. Kim, D. A. Cullen, D. Zheng, P. Li, M. Shakouri, E. Heredia, P. Cui, H. N. Alshareef, Y. Hu and H. Wang, *Nat. Chem.*, 2021, **13**, 887–894.

52 G. Henkelman, A. Arnaldsson and H. Jónsson, *Comput. Mater. Sci.*, 2006, **36**, 354–360.

53 C. Ling, Y. Ouyang, Q. Li, X. Bai, X. Mao, A. Du and J. Wang, *Small Methods*, 2019, **3**, 1800376.

54 S. Garcia-Segura, M. Lanzarini-Lopes, K. Hristovski and P. Westerhoff, *Appl. Catal., B*, 2018, **236**, 546–568.

55 S. Kattel, P. Atanassov and B. Kiefer, *J. Phys. Chem. C*, 2012, **116**, 8161–8166.

56 X.-F. Li, Q.-K. Li, J. Cheng, L. Liu, Q. Yan, Y. Wu, X.-H. Zhang, Z.-Y. Wang, Q. Qiu and Y. Luo, *J. Am. Chem. Soc.*, 2016, **138**, 8706–8709.

57 D. Wu, B. He, Y. Wang, P. Lv, D. Ma and Y. Jia, *J. Phys. D: Appl. Phys.*, 2022, **55**, 203001.

58 V. L. Deringer, A. L. Tchougréeff and R. Dronskowski, *J. Phys. Chem. A*, 2011, **115**, 5461–5466.

59 A. J. Medford, A. Vojvodic, J. S. Hummelshøj, J. Voss, F. Abild-Pedersen, F. Studt, T. Bligaard, A. Nilsson and J. K. Nørskov, *J. Catal.*, 2015, **328**, 36–42.

60 J. Greeley, T. F. Jaramillo, J. Bonde, I. Chorkendorff and J. K. Nørskov, *Nat. Mater.*, 2006, **5**, 909–913.

61 A. Kulkarni, S. Siahrostami, A. Patel and J. K. Nørskov, *Chem. Rev.*, 2018, **118**, 2302–2312.

62 H. Li, C. Tsai, A. L. Koh, L. Cai, A. W. Contryman, A. H. Fragapane, J. Zhao, H. S. Han, H. C. Manoharan, F. Abild-Pedersen, J. K. Nørskov and X. Zheng, *Nat. Mater.*, 2016, **15**, 48–53.

63 B. Hammer, Y. Morikawa and J. K. Nørskov, *Phys. Rev. Lett.*, 1996, **76**, 2141–2144.

64 M. Mavrikakis, B. Hammer and J. K. Nørskov, *Phys. Rev. Lett.*, 1998, **81**, 2819–2822.

65 V. Stamenkovic, B. S. Mun, K. J. J. Mayrhofer, P. N. Ross, N. M. Markovic, J. Rossmeisl, J. Greeley and J. K. Nørskov, *Angew. Chem., Int. Ed.*, 2006, **45**, 2897–2901.

66 J. K. Nørskov, F. Abild-Pedersen, F. Studt and T. Bligaard, *Proc. Natl. Acad. Sci. U. S. A.*, 2011, **108**, 937–943.

67 H. Xu, D. Cheng, D. Cao and X. C. Zeng, *Nat. Catal.*, 2018, **1**, 339–348.

68 K. Jiang, S. Siahrostami, T. Zheng, Y. Hu, S. Hwang, E. Stavitski, Y. Peng, J. Dynes, M. Gangisetty, D. Su, K. Attenkofer and H. Wang, *Energy Environ. Sci.*, 2018, **11**, 893–903.

69 P. H. van Langevelde, I. Katsounaros and M. T. M. Koper, *Joule*, 2021, **5**, 290–294.